pp 1476–1491. © Royal Aeronautical Society 2019
doi:10.1017/aer.2019.68

Horizontal tail local angle-of-attack and total pressure measurements through static pressure ports and Kiel pitot

R. M. Granzoto
rodrigo.granzoto@embraer.com.br
Embraer S.A.
São José dos Campos
Brazil

L. A. Algodoal
Embraer S.A.
São José dos Campos
Brazil

G. J. Zambrano
Embraer S.A.
São José dos Campos
Brazil

G. G. Becker
Embraer S.A.
São José dos Campos
Brazil

ABSTRACT

Aircraft handling qualities may be influenced by wing-tip flow separations and horizontal tail (HT) reduced efficiency caused by loss of local dynamic pressure or local tailplane flow separations in high angle-of-attack manoeuvres. From the flight tester's perspective, provided that the test aircraft presents sufficient longitudinal control authority to overcome an uncommanded nose-up motion, this characteristic should not be a safety factor. Monitoring and measuring the local airflow in the aircraft's HT provides information for safe flight-test envelope expansion and data for early aerodynamic knowledge and model validation. This work presents the development, installation and pre-flight calibration using computational fluid dynamics (CFD), flight-test calibration, results and benefits of differential pressure based

Received 27 April 2018; revised 13 March 2019; accepted 14 June 2019.
A version of this paper was presented at the 31st ICAS Congress of the International Council of the Aeronautical Sciences in Belo Horizonte, Brazil in September 2018.

local angle-of-attack and total pressure measurements through 20 static pressure ports and a Kiel pitot. These sensors were installed in a single-aisle, four-abreast, full fly-by-wire medium-range jet airliner with twin turbofan engines and conventional HT (low vertical position).

Keywords: Aerodynamics; CFD; flight-test; horizontal tail; angle-of-attack; sensor calibration

NOMENCLATURE

C_P	Non-dimensional coefficient of differential pressure
CG	Centre of Gravity
CFD	Computer fluid dynamics
HT	Horizontal Tail
I_{HT}	Horizontal tail incidence angle
K_1	Calibration factor
n	Pressure tap number
P_{ref}	Reference absolute static pressure
P_∞	Free-stream static pressure
Q_∞	Free-stream dynamic pressure
s	Measurement section along HT span
t	Instantaneous time
α	Free-stream angle-of-attack
α_{HT}	Local HT angle-of-attack
α_{HT1}	Effect of local Cp distribution on HT angle-of-attack
α_{HT1A}	Effect of local Cp distribution on HT angle-of-attack of section A
α_{HT1B}	Effect of local Cp distribution on HT angle-of-attack of section B
α_{HT2}	Effect of wing interference HT angle-of-attack
α_{HT2A}	Effect of wing interference HT angle-of-attack of section A
α_{HT2B}	Effect of wing interference HT angle-of-attack of section B
α_{HT3}	Effect of local HT incidence interference on HT angle-of-attack
α_{HT3A}	Effect of local HT incidence interference on HT angle-of-attack of section A
α_{HT3B}	Effect of local HT incidence interference on HT angle-of-attack of section B
$\Delta\alpha_{HT}$	Difference in local angle-of-attack between two different conditions
$\Delta\alpha_{HTdyn}$	Increase in local HT angle-of-attack due to pitch rate
ΔI_{HT}	Difference in HT incidence between two different conditions
Δ_{Pn}	Differential pressure measured at each static port relative to P_{ref}
ε	Wing downwash angle
ε_0	Wing downwash angle for zero angle-of-attack
$\varepsilon/d\alpha$	Wing downwash angle slope
δ_e	Elevator deflection
δ_{flap}	Flap deflection
η	Ratio between the free-stream and HT local dynamic pressure
τ	Wing downwash lag due to α rate

https://doi.org/10.1017/aer.2019.68 Published online by Cambridge University Press

1.0 INTRODUCTION

As an important part of the preparation for the high incidence envelope expansion flight-test campaign, the aircraft longitudinal stability and the possible tendency for uncommanded pitch movements must be considered. Newer aircraft models with increased aspect ratio and swept wings, higher efficiency flaps, higher bypass engines (increased diameter) and, finally, lower horizontal tail (HT) area combined with more aft centre-of-gravity (CG) positions have led to a concern over achieving more critical stability and controls characteristics during stall manoeuvres. Particularly, the aircraft handling qualities characteristics may be influenced by wing-tip flow separations and HT-reduced efficiency caused by loss of local dynamic pressure or local tailplane flow separations in high angle-of-attack manoeuvres.

From the flight tester's perspective, provided the test aircraft presents sufficient longitudinal control authority to overcome an eventual uncommanded nose up motion, these characteristics should not be a safety factor.

Once the flight mechanics analysis of the test aircraft showed the longitudinal control authority to be safe enough to cope with all the test conditions, there will still be the need for real-time monitoring during the test execution to assure the assumptions and the models used for all the previous analysis were valid.

Two key parameters have been successfully used in flight to accomplish this need for real-time monitoring:

- HT local angle-of-attack (α_{HT}); and
- Dynamic pressure measurements, particularly the ratio between the free-stream dynamic pressure and the HT local dynamic pressure (η).

The first one (α_{HT}) copes with the risk of reaching a tailplane stall, which decreases the aircraft's longitudinal stability and may lead to an uncommanded pitch movement. The second one (η) copes with a possible reduction in longitudinal stability and control authority of a non-stalled tail due to low dynamic pressure (i.e. due to engine or wing-flow paths passing thought the tail position).

Monitoring and measuring the local airflow in the aircraft's HT provides, thus, information for safe flight-test envelope expansion and data for early aerodynamic knowledge and model validation.

This work presents the development, installation, pre-flight calibration using computational fluid dynamics (CFD), flight-test calibration, results and benefits of angle-of-attack estimation based on 20 static pressure ports and total pressure measurements through a Kiel pitot.

These sensors were installed in a single-aisle, four-abreast, full fly-by-wire medium-range jet airliner with twin turbofan engines and conventional HT (low vertical position).

2.0 SENSORS INSTALLATION

Once identified the need for real-time monitoring of HT local angle-of-attack, several options of different sensors were considered[1]. Most of the available sensors, such as angle-of-attack vanes, smart probes, etc. would have similar calibration challenges but would significantly affect the HT structural characteristics; in addition, most of the already available sensors, due to their size and ideal locations were considered to interfere with the local airflow, thus interfering with the local α_{HT} measurement itself.

The search for a local angle-of-attack measurement that would not significantly affect the HT structural design and be non-airflow-interferant led to a differential static pressure

https://doi.org/10.1017/aer.2019.68 Published online by Cambridge University Press

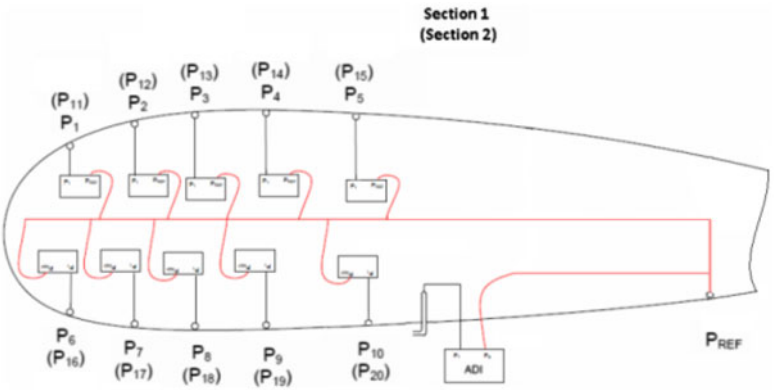

Figure 1. Schematic system architecture of the system.

solution. This solution only requires small pressure ports (small holes) adequately located to be sensible to small pressure differences between the upper and lower surfaces of the HT aerofoil. Those differential pressure measures are physically correlated to local angle-of-attack variations.

The static pressure ports were designed to be located on the leading edge of the HT. This location was chosen due to two different aspects:

1. It presents a higher sensitivity of static pressure coefficient (C_P) due to α_{HT} variation.
2. Ease of installation and maintenance, once the pressure transducers can be installed with the removal of the HT leading edge, which is usually removable in most aircraft for several other reasons (for example, anti-ice piccolo tubes installation).

As the differential pressure ports are susceptible to blockage and local disturbances and considering the safety effects of a wrong measure for real-time monitoring during the flight test, a conservative, robust and redundant design was chosen: the differential pressure ports were distributed along ten chord positions for two distinct sections along the HT span. For this purpose, an averaging and a voting algorithm were employed for the final α_{HT} measurement.

Figure 1 shows the schematic architecture of the system.

Considering the needs for a quick time response, good accuracy and resolution, the Honeywell PPT0002DNN2VB-S068 differential pressure sensor was chosen.

Honeywell PPT0002DNN2VB-S068 specifications[(2)]:
Digital Accuracy: ±0.05% FS
Analog Accuracy: ±0.06% FS
Operating Temperature: −40 to 85°C
Storage Temperature: −55 to 90°C
Sample Rate: 8.33ms to 51.2min
Digital Resolution: up to ±0.0011% FS
Analog Resolution: 1.22mV
Long Term Stability: 0.025% FS per year
Range: ±2 psi

Since the PPT0002DNN2VB-S068 needs to be connected to the reference pressure using capillary tubes, to avoid a possible pressure wave lag in the final measure, a single static

https://doi.org/10.1017/aer.2019.68 Published online by Cambridge University Press

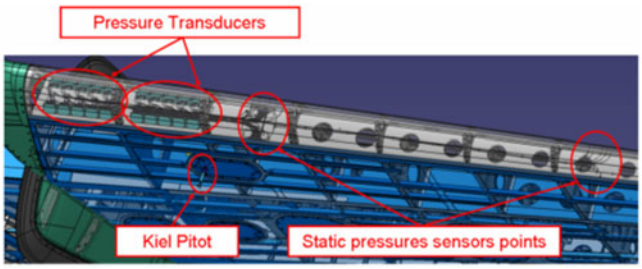

Figure 2. HT sensors positions and installation.

pressure (P_{ref}) reference port was chosen and positioned as close as possible to transducers minimising the tubes length and consequently its internal air volume. The P_{ref} was in the lower side of HT.

All 20 differential pressure transducers are connected to a reference static pressure port (P_{ref}). Consequently, each transducer measures a differential pressure ΔP_n relative to the reference static port P_{ref}.

It is possible to convert the measure from the reference point to free-stream values by Equation (1), which uses free-stream static pressure (P_∞) and dynamic pressure (Q_∞). These quantities may be provided by the aircraft's anemometric system or measured by dedicated flight-test instrumentation sensors, such as a trailing cone and aircraft Kiel pitot.

$$C_{P_n} = \frac{\Delta P_n + P_{ref} - P_\infty}{Q_\infty} \quad \ldots (1)$$

The local dynamic pressure was measured through a Kiel pitot installed on the lower side of the HT using a pre-existent access panel for the ease of installation and maintenance. The Kiel pitot vertical position was chosen to keep it out of the boundary layer.

Figure 2 provides detailed information for the position of installed pressure ports, pressure transducers and Kiel pitot.

3.0 PRE-FLIGHT SENSORS CALIBRATION

The adopted differential pressure solution does not provide a direct local angle-of-attack measurement, thus, requiring the means to convert differential pressure measurements in angle-of-attack.

To develop the proper correlation between differential pressure and local angle-of-attack, an estimation of the α_{HT} (pre-flight) was done using CFD.

In order to derive the relations, CFD simulations were performed with Metacomp Technologies CFD++ code[3] to simulate subsonic airflow conditions.

Three different types of CFD simulations were run:

- Complete aircraft (WBPNH) with HT incidence variation;
- Wing-Body-Pylon-Nacelle tailless aircraft (WBPN);
- Body-Horizontal-Tail (BH) wingless aircraft with different elevator deflections.

The grids are generated using the gridding guidelines based on the EMBRAER experience[4]. The flow is modelled using the Reynolds-averaged Navier-Stokes equations (RANS) with turbulence model closures. The time march is performed using a point-implicit method

https://doi.org/10.1017/aer.2019.68 Published online by Cambridge University Press

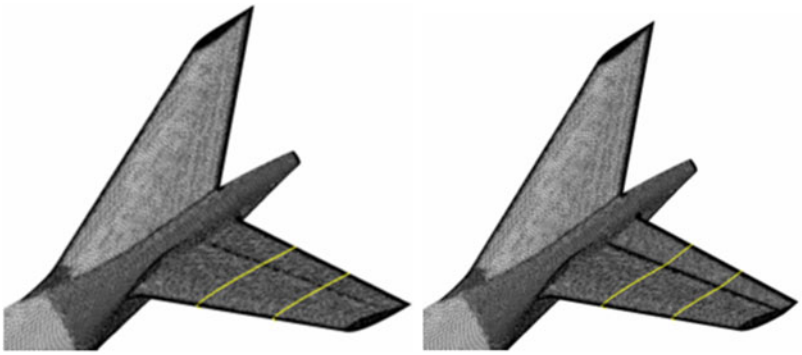

Figure 3. Body-Horizontal-Tail mesh – with elevator two different elevator deflections.

and multigrid method for convergence acceleration. In this work, the SA turbulence model is employed[5] and is a well-established closing model for aerospace industrial applications.

Local α_{HT} for each section takes into consideration the three effects (α_{HT1}, α_{HT2} and α_{HT3}) according to Equation (2).

$$\alpha_{HT_S} = \alpha_{HT1_S} + \alpha_{HT2_S} + \alpha_{HT3_S} \quad \ldots (2)$$

Where:
S denotes the HT section (1 or 2) and the terms are:

TERM α_{HT1}

The α_{HT1} is the direct correlation between differential pressure measurements and local angle-of-attack. This correlation for each section S is a function of C_P and elevator deflection. The final α_{HT1} is the mean of the values calculated for each of the ten sensors, Equation (3). Figure 3 shows Body and Horizontal Tail mesh with two different elevator deflections.

$$\alpha_{HT1_S} = f(C_{Pn}, \delta_e) = \frac{1}{10} \times \sum_{n=1}^{10} \alpha_{HT1n} \quad \ldots (3)$$

The Body-Horizontal-Tail (BH) CFD results were post-processed to provide α_{HT1}, i.e. the direct correlation between differential pressure and local angle-of-attack, for different elevator angles. For each pressure port location, a local angle-of-attack α_{HT1} was derived as a function of C_P and elevator deflection. As these runs have no wing effect, the HT angle-of-attack is the same as free-stream angle-of-attack. Figure 4 shows the correlation between C_P and α_{HT1} for the five pressure ports at upper side of HT in the section 1 with zero elevator deflection.

TERM α_{HT2}

The α_{HT2} is a function of aircraft free-stream angle-of-attack (α) and flap deflection angle (δ_{flap}), since the wing lift and downwash interferes with local HT airflow and changes the chordwise and spanwise distribution of local lift on HT.

$$\alpha_{HT2_S} = f(\alpha, \delta_{flap}) \quad \ldots (4)$$

The α_{HT2} was calculated using WBPN CFD runs (without HT) with wing interference results calculated at 25% of local HT chord virtual position for each spanwise HT section, as it may be seen by Fig. 5. Figure 6 shows the local α spanwise distribution as a function of free-stream a for the landing flaps configuration.

https://doi.org/10.1017/aer.2019.68 Published online by Cambridge University Press

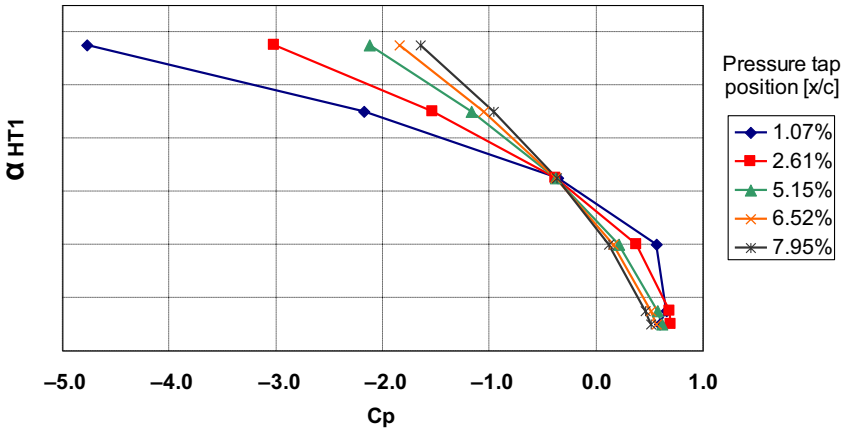

Figure 4. Example of α_{HT1} as function of C_P for some pressure taps.

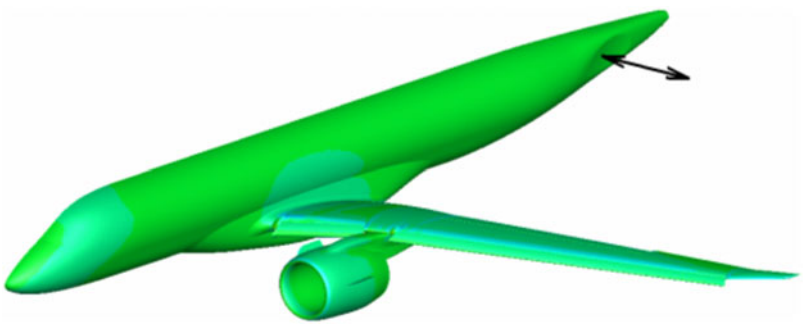

Figure 5. Wing-Body-Pylon-Nacelle configuration CFD runs showing wing and engine effects on local virtual HT position.

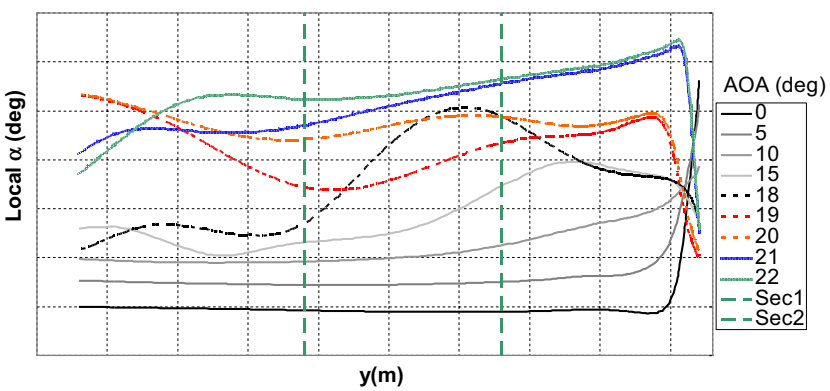

Figure 6. Local angle-of-attack at virtual HT position as a function of span position for various aircraft angle-of-attack – Landing flaps configuration.

https://doi.org/10.1017/aer.2019.68 Published online by Cambridge University Press

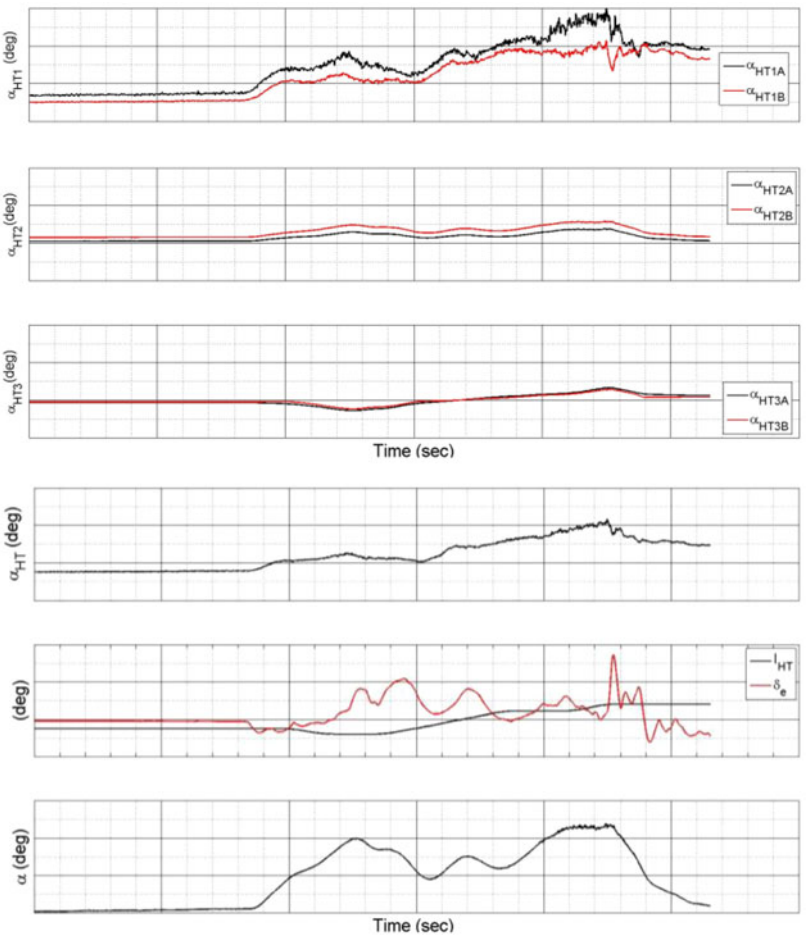

Figure 7. α_{HT} components contribution comparison during a flight-test stall manoeuvre.

TERM α_{HT3}

α_{HT3} is a function of HT incidence (α_{HT3}), since the relative geometric position of the HT changes the aerodynamic interference characteristics between wing-tail and fuselage-tail, thus changing local HT pressure distribution. The α_{HT3} for each section is an interference correction, which is a function of free-stream angle-of-attack, flap deflection angle and HT incidence.

$$\alpha_{HT3_S} = f(\alpha, \delta_{flap}, I_{HT}) \quad \ldots (5)$$

The α_{HT3} was calculated through CFD runs with WBPNH configuration with I_{HT} incidences of 0°, −3° and −6°, thus providing corrections for the interference due to the local geometric incidence.

The final value of α_{HT} is the mean of the calculated values for each of the two spanwise sections.

$$\alpha_{HT} = \frac{1}{2} \times \sum_{S=1}^{2} \alpha_{HT_S} \quad \ldots (6)$$

https://doi.org/10.1017/aer.2019.68 Published online by Cambridge University Press

Figure 7 compares α_{HT} components contribution during a stall manoeuvre. The plot shows that α_{HT1} is the most significant component when compared to α_{HT2} and α_{HT3} by one order of magnitude. That is because α_{HT2} and α_{HT3} are interference corrections factors, and α_{HT1} is directly correlated to C_P.

4.0 FLIGHT-TEST CALIBRATION

The flight-test calibration of α_{HT} was based on the principle that when the aircraft angle-of-attack is kept constant, wing downwash may also be assumed constant. If it is possible to change HT incidence without changing aircraft angle-of-attack, the resultant change in HT incidence (ΔI_{HT}) should be equal to the change in local angle-of-attack ($\Delta\alpha_{HT}$).

The flight-test procedure was based on the following steps:

- Trim the aircraft in a specified condition.
- Jam the elevator from the same side of sensors installation in a specified condition using a pre-defined function of flight-controls computer.
- Mistrim the aircraft using the trim switch and control the aircraft using the opposite side elevator to compensate for the mistrim. This elevator is not jammed and does not influence the pressure sensors because it is not located in the same side of the pressure sensors.
- Keep airspeed and aircraft angle-of-attack constant during manoeuvre.

For static conditions, local α_{HT} is a function of aircraft downwash and local tail incidence. Equations (7) and (8) describe, respectively, the conditions before and after the aircraft is mistrimmed.

$$\alpha_{HT1} = \alpha_1 - \varepsilon_1 + I_{HT1} \quad \ldots (7)$$

$$\alpha_{HT2} = \alpha_2 - \varepsilon_2 + I_{HT2} \quad \ldots (8)$$

The flight-test calibration manoeuvre is performed varying the I_{HT} and keeping the remaining parameters constant, thus:

$$\alpha_1 = \alpha_2 \quad \ldots (9)$$

$$\varepsilon_1 = \varepsilon_2 \quad \ldots (10)$$

Subtracting Equation (7) from Equation (8) results:

$$\alpha_{HT1} - \alpha_{HT2} = I_{HT1} - I_{HT2} \quad \ldots (11)$$

$$\Delta\alpha_{HT} = \Delta I_{HT} \quad \ldots (12)$$

The quantities ΔI_{HT} and $\Delta\alpha_{HT}$ may be calculated in relation to trimmed initial condition. Because Equation (12) is not satisfied exactly in flight-test conditions, a calibration factor, K_1 is introduced, as shown in Equation (13).

$$\Delta I_{HT} = K_1 \times \Delta\alpha_{HT} \quad \ldots (13)$$

https://doi.org/10.1017/aer.2019.68 Published online by Cambridge University Press

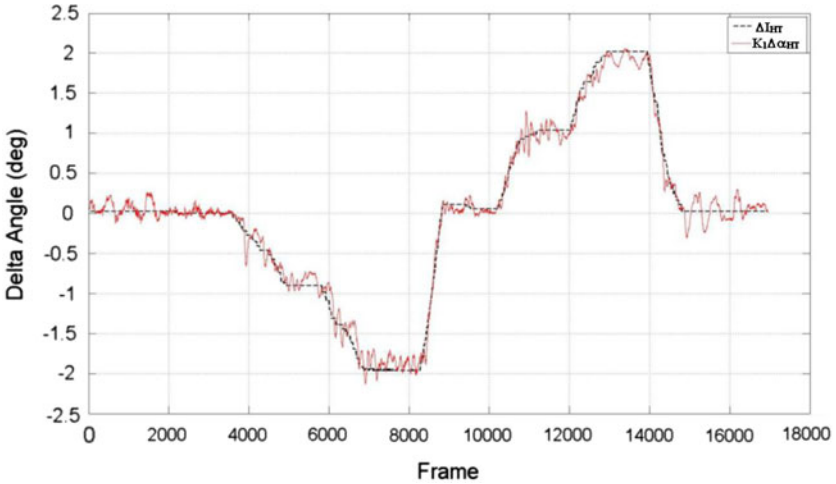

Figure 8. Calibration flight-test results – comparison between ΔI_{HT} and $K_1 \Delta\alpha_{HT}$ – Cruise Flaps Configuration.

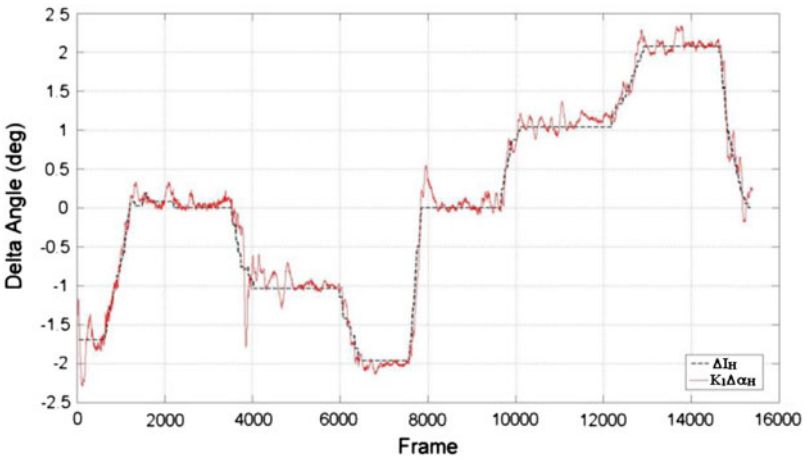

Figure 9. Calibration flight-test results – comparison between ΔI_{HT} and $K_1 \Delta\alpha_{HT}$ – Take-off Flaps Configuration.

This process is repeated for each elevator position, thus providing corrections for the direct relationship between local angle-of-attack, elevator deflection and local C_P. This process is also repeated for different angle-of-attacks and flap deflections and, consequently, provides corrections to the interference between wing and HT.

A flight data comparison between ΔI_{HT} and $K_1 \times \Delta\alpha_{HT}$ is presented in Figs 8, 9 and 10. The good correlation shows that the calibration factor was sufficient to capture the effects of wing interference and local pressure distribution for different elevator deflections. It is important the calibration has good physics modelling to increase the correlation between theoretical and flight-test data.

https://doi.org/10.1017/aer.2019.68 Published online by Cambridge University Press

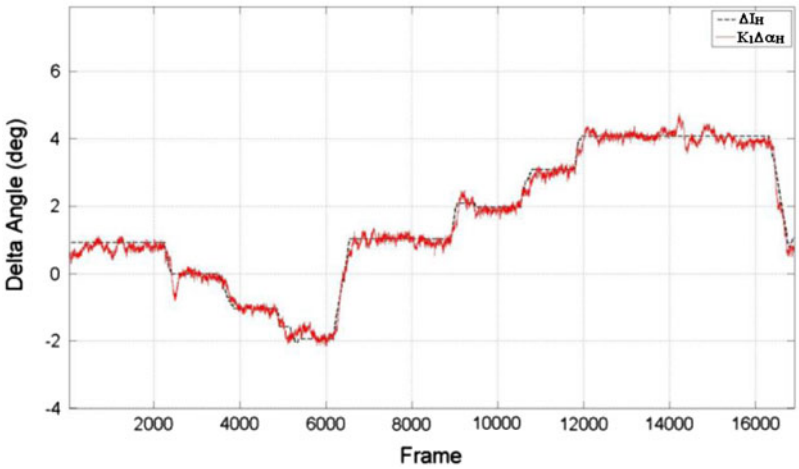

Figure 10. Calibration flight-test results – comparison Between ΔI_{HT} and $K_1 \Delta \alpha_{HT}$ – Landing Flaps Configuration.

5.0 FLIGHT-TEST RESULTS

The local HT angle-of-attack and dynamic pressure and the wing downwash are physically correlated to the aircraft inherent aerodynamic stability.

In the earlier stages of aircraft development, before first flight, wind-tunnel data is used to predict α_{HT} and ε. These data are also fed into flight dynamics simulation models to evaluate the aircraft handling characteristics, function hazard analysis, design, etc. It is important to understand how the measured variables compare to predictions based on wind-tunnel data in the early stages of aircraft flight-test development for safe envelope expansion and for aircraft control laws development and validation.

The differences between flight-test and wind-tunnel data may be used to improve existent flight-mechanics models. Data may be extrapolated for the more critical conditions, such as higher angle-of-attack and aft CG stall manoeuvres. These new predicted data then may be compared with real-time measurements of ε and α_{HT} during stall manoeuvres, providing safe flight-test stop criteria if these parameters are out of a pre-determined range.

In aircraft with fly-by-wire systems, the control laws may be susceptible to aerodynamic model errors, particularly in the higher α region. The downwash and local-angle-of-attack measurements may also be used in conjunction with parameter-estimation techniques to improve linear models used when updating controls laws gains. The early update of flight-controls laws is important to improve flight-test efficiency and to provide safer flight-test expansion.

During the stall manoeuvres, the wing downwash (ε) may be computed for each time (t) step as a function of wing angle-of-attack (α), measured local angle-of-attack (α_{HT}) and HT incidence (I_{HT}). If the manoeuvre is not quasi-static, i.e. with high pitch and α rates, the downwash lag (τ) and the increase in local HT α due to the pitch rate (α_{HTdyn}) shall be considered:

$$\varepsilon(t-\tau) = \alpha(t) - \alpha_{HT}(t) + \alpha_{HTdyn}(t) + I_{HT}(t) \quad \ldots (14)$$

Figure 11 shows such an example of computation that may be calculated in real-time during the execution of stall manoeuvres. It shows a time-history comparison between flight-test and

https://doi.org/10.1017/aer.2019.68 Published online by Cambridge University Press

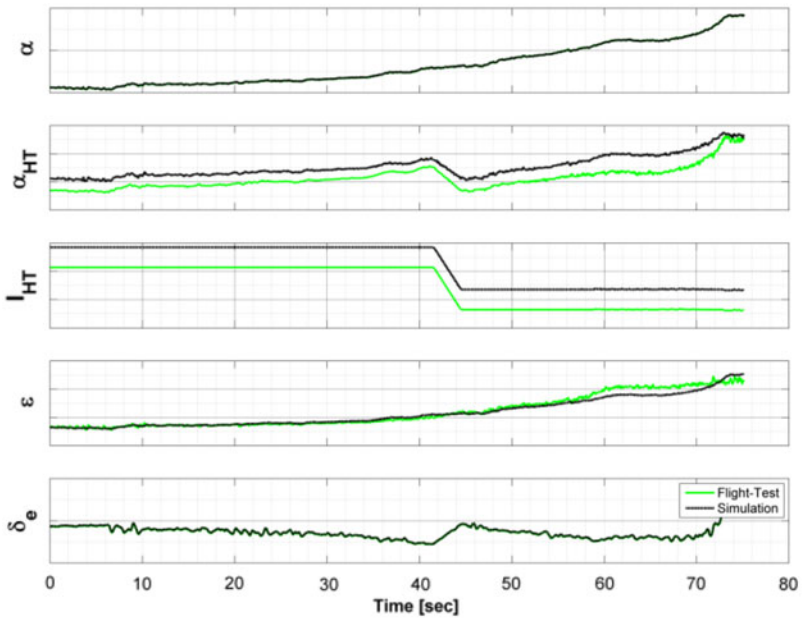

Figure 11. α_{HT} and ε comparison between simulation based on wind tunnel data and flight-test data during a stall manoeuvre – Cruise Flaps Configuration.

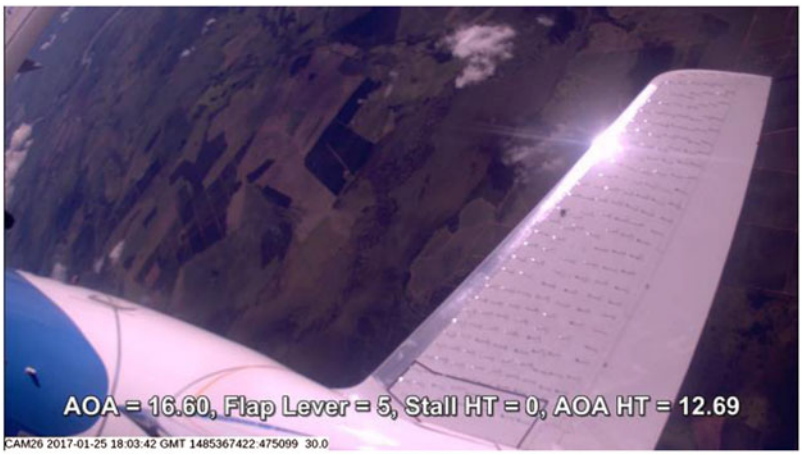

Figure 12. Tufts flow visualisation combined with HT measurements during a high incidence flight-test manoeuvre.

wind-tunnel simulation data for the parameters angle-of-attack, downwash, local HT angle-of-attack, HT incidence and elevator deflection.

The measurement of HT characteristics was also combined with flow visualisation techniques to provide information for validation and understanding of the aerodynamic characteristics of HT airflow. Figure 12 shows the flow visualisation using tufts combined with measurements of HT angle-of-attack during a high incidence flight-test manoeuvre.

https://doi.org/10.1017/aer.2019.68 Published online by Cambridge University Press

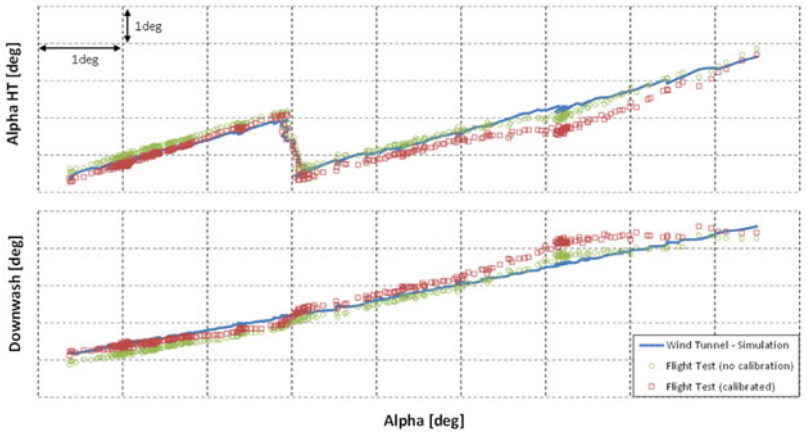

Figure 13. Local α_{HT} and downwash comparison between wind-tunnel data and flight-test data during a stall manoeuvre – Cruise Flaps Configuration.

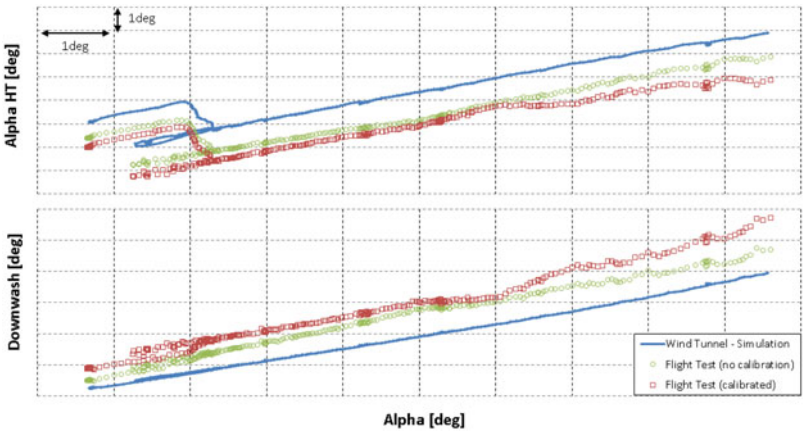

Figure 14. Local α_{HT} and downwash comparison between wind-tunnel data and flight-test data during a stall manoeuvre – Low Take-off Flaps Configuration.

Crossplots of wing downwash and aircraft angle-of-attack are shown in Figs 13 to 16 for cruise, low take-off, high take-off and landing flaps configurations. The plots compare flight-test data (with and without calibration) with wind-tunnel data.

The results show that the differences between flight-test and wind-tunnel data increase for higher angles-of-attack, probably due to higher interferences caused by wing and engine flow over the HT. These interferences may have different aerodynamic behaviour between wind-tunnel and flight-test (due to inherent wind-tunnel limitations such as geometric and Reynolds number differences) and may affect the measurement and calibration of α_{HT} itself.

The dynamic pressure ratio as a function of aircraft angle-of-attack is shown in Figs 17 to 20 for cruise, low take-off, high take-off and landing flaps configurations.

The results show a significant loss of dynamic pressure at medium angles-of-attack, which decreases aircraft longitudinal stability and elevator efficiency. However, in the more deflected flaps configurations, which are the critical conditions for stall characteristics, the local

https://doi.org/10.1017/aer.2019.68 Published online by Cambridge University Press

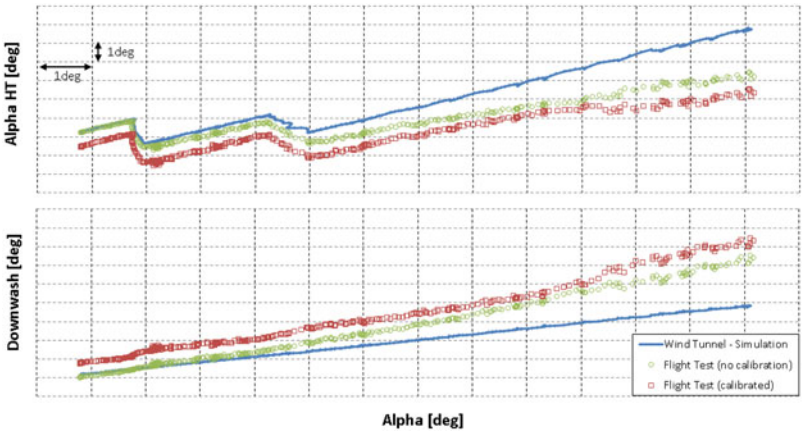

Figure 15. Local α_{HT} and downwash comparison between wind-tunnel data and flight-test data during a stall manoeuvre – High Take-off Flaps Configuration.

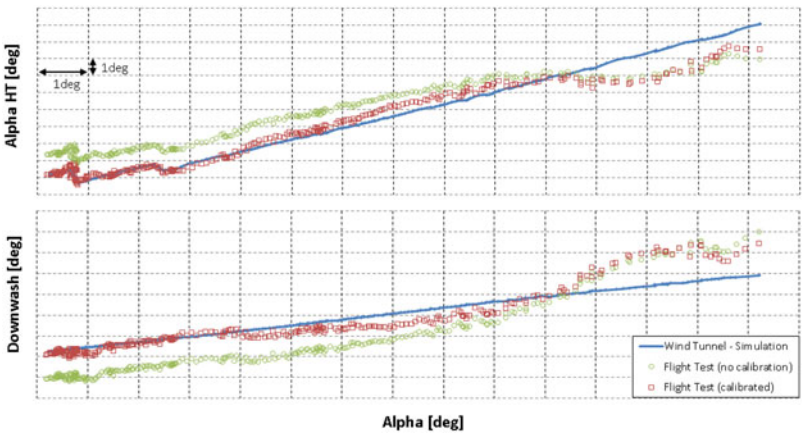

Figure 16. Local α_{HT} and downwash comparison between wind-tunnel data and flight-test data during a stall manoeuvre – Landing Flaps Configuration.

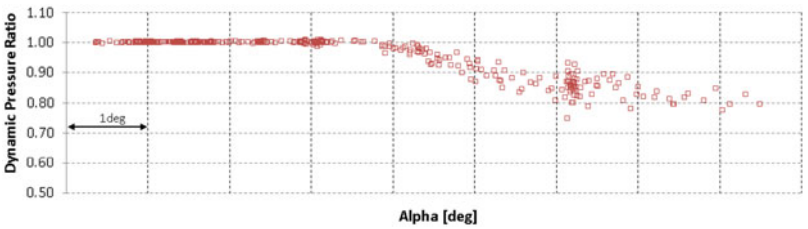

Figure 17. Flight-test measurement of dynamic pressure ratio between local and global dynamic pressure (η) – Cruise Flaps Configuration.

https://doi.org/10.1017/aer.2019.68 Published online by Cambridge University Press

Table 1
Differences between flight-test results and estimated wind-tunnel parameters ε_0 and $d\varepsilon/d\alpha$

Configuration	Error on ε_0	Error on $d\varepsilon/d\alpha$
Cruise Configuration	0.4 deg	12.0%
Low Take-off Configuration	−0.6 deg	8.5%
High Take-off Configuration	0.2 deg	30.7%
Landing Configuration	−0.2 deg	18.8%

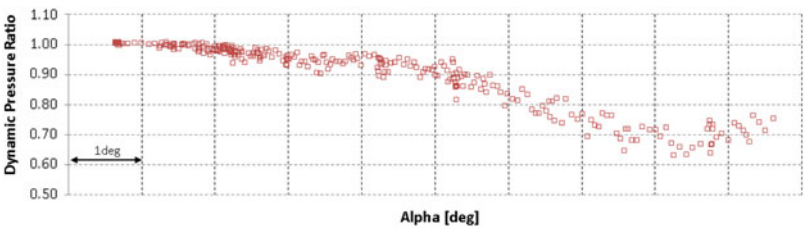

Figure 18. Flight-test measurement of dynamic pressure ratio between local and global dynamic pressure – Low Take-off Flaps Configuration.

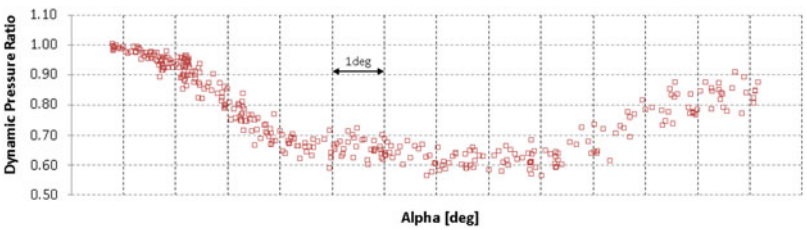

Figure 19. Flight-test measurement of dynamic pressure ratio between local and global dynamic pressure (η) – High Take-off Flaps Configuration.

dynamic pressure starts to increase again near the stall angle-of-attack, improving stability and control characteristics.

If such curves of Figs 13 to 16 are linearized in the linear region of each curve, the wing downwash (ε) may be written as a function of downwash for zero angle-of-attack (ε_0) and a downwash slope ($d\varepsilon/d\alpha$), as in Equation (15).

$$\varepsilon = \varepsilon_0 + {}^{d\varepsilon}/_{d\alpha} \quad \ldots (15)$$

Table 1 compares the linearized downwash parameters between flight-test and wind-tunnel data.

In general, the differences between flight-test and wind-tunnel data (both in the linear and non-linear region) have shown that the expected maximum α_{HT} that would be achieved in the most critical manoeuvres would always be less than the simulations model predicted, providing a safety margin for envelope expansion.

https://doi.org/10.1017/aer.2019.68 Published online by Cambridge University Press

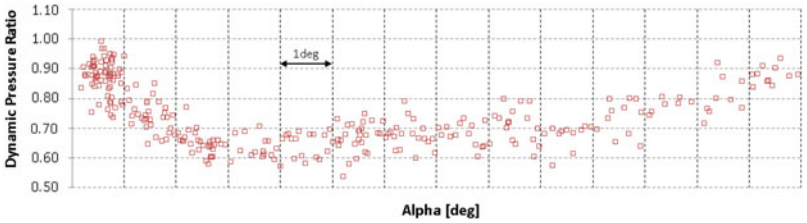

Figure 20. Flight-test measurement of dynamic pressure ratio between local and global dynamic pressure (η) – Landing Flaps Configuration.

6.0 CONCLUSIONS

The choice of differential pressure-based local HT angle-of-attack measurement showed the following advantages:

- Ease of installation;
- No interference in the local airflow;
- Good correlation with theoretical data;
- Safe monitoring of an entire high angle-of-attack flight-test campaign;
- Ease of in-flight calibration procedure;
- Robustness to sensor port blockage (redundancy);
- Aerodynamics characteristics of flight-test aircraft in conformity with production aircraft.

The disadvantages observed during the use and operation of this sensor was:

- Sensitiveness to high moisture environment because of the sensor's blockage;
- Non-suitability for use in the artificial ice shapes tests (due to installation of simulated ice shapes in the leading edge of the test aircraft HT).

REFERENCES

1. EPPEL, J.C., RIDDLE, D.W. and STEVES, V.C. *Flight Measured Downwash of the QSRA*, Ames Research Center, 1988, Moffett Field, California.
2. Honeywell Precision Pressure Transducer (PPT) Data Sheet.
3. 'CFD++ Documentation', Metacomp Technologies Inc., retrieved from http://www.metacomptech.com, accessed in March 2017.
4. SCALABRIN, L.C., CILONI, P., ANTUNES, A., BECKER, G.G., SOUZA, M.A., and GRANZOTO, R.M. EMBRAER Contribution to HiLiftPW-3, 2018 AIAA Aerospace Sciences Meeting, AIAA SciTech Forum, (AIAA 2018-1036).
5. SPARLAT, P. R. Strategies for turbulence modelling end simulations, *International J Heat and Fluid Flow*, 2000, **21**, pp 252–263.

https://doi.org/10.1017/aer.2019.68 Published online by Cambridge University Press